

Ultrathin, Flexible, and Transparent Oxide Thin-Film Transistors by Delamination and Transfer Methods for Deformable Displays

Jong Beom Ko, Seung Hee Lee, Tae-Ik Lee, Sangmin Lee, Jingyu Kim, Hyeok Kim, Taek-Soo Kim, and Sang-Hee Ko Park*

The attachment of display devices to various objects has attracted much attention due to their ability to present visual information to people in different environments. Such devices should be ultrathin to ensure complete coverage when attached to various objects, making them a critical technology for the development of rollable and stretchable displays. In this study, the fabrication of high-performance ultrathin oxide thin-film transistors (TFTs) on a 5 μm -thick polyethylene terephthalate substrate is demonstrated by the method of delamination and transfer. Molybdenum oxide functions as an exfoliation layer, and the ultrathin devices exhibit full coverage on various objects with complex surface profiles such as contact lens, fabric, and human skin. It is notable that the TFT device exhibits a high optical transparency of greater than 81% and a reasonable electrical performance with a high mobility of $37 \text{ cm}^2 \text{ V}^{-1} \text{ s}^{-1}$. Since the oxide TFTs are fabricated without temperature limitations, the devices show reliable electrical performances under gate and illumination stresses. The flexible devices also exhibit excellent transfer characteristics in the bending state, regardless of the bending radius and direction, as well as a high mechanical durability of over 10 000 bending cycles with the bending radius of 3 mm.

applications such as in wearable devices, glasses of transportation and buildings, and mirrors.^[1–3] The transparent organic light-emitting diodes (OLEDs) and micro-light emitting diodes (micro-LEDs) are the optimal candidates among the various display devices for the aforementioned applications. This is attributed to the outstanding performances and relatively high power efficiencies of the OLEDs and micro LEDs.^[4,5] Furthermore, backplane devices play a critical role in the development of next-generation displays.

Thin-film transistors (TFTs) are utilized as the backplane devices for active matrix (AM) liquid-crystal displays, AM organic light-emitting diode (AMOLED) displays, AM-LEDs, and quantum-dot LEDs. TFTs with amorphous oxide semiconductors are suitable candidates for such applications owing to their multiple advantages such as ease of fabrication, high electron mobility, high electrical stability, and uniformity

over a large area.^[6,7] Therefore, it is necessary to develop flexible and transparent oxide TFTs that exhibit outstanding electrical performances. Furthermore, it is essential to design ultrathin display devices to ensure their complete coverage on and attachment to various objects including stretchable substrates.

A typical fabrication method for flexible oxide TFTs includes a direct formation of film on a plastic substrate by a vapor deposition, solution spinning, or bar coating, followed by photopatterning.^[8–10] However, most of the transparent plastic films, including polyethylene terephthalate (PET) exhibit a high coefficient of thermal expansion and a low glass transition temperature (T_g).^[11] These characteristics hinder the optimization of the electrical performance of the oxide thin films that can be achieved by post-annealing at high temperatures. Furthermore, they also prevent the high-density integration of devices. To address these drawbacks, extensive research has been conducted on the application of heat-resistant plastic films like polyimide as flexible substrates.^[12–14] However, these films exhibit a low optical transparency owing to their yellowish appearance. Although the colorless polyimide can be processed at 300 °C as a substrate for oxide TFTs, the thick thickness (>10 μm) of such devices prevents their applications to substrates with diverse surface profiles.

To alleviate these issues, ultrathin flexible devices were prepared by a technique involving delamination and transfer, where the TFT arrays were delaminated from a rigid substrate

1. Introduction

Deformable such as multi-foldable, rollable, and stretchable displays have attracted significant attention owing to their diverse

Dr. J. B. Ko, S. H. Lee, J. Kim, Prof. S.-H. K. Park
Department of Materials Science and Engineering
Korea Advanced Institute of Science and Technology (KAIST)
291 Daehak-ro, Yuseong-gu, Daejeon 34141, Republic of Korea
E-mail: shkp@kaist.ac.kr

Dr. T.-I. Lee
Joining R&D Group
Korea Institute of Industrial Technology (KITECH)
156 Gaetbeol-ro, Yeosu-gu, Incheon 21999, Republic of Korea

Dr. S. Lee, Prof. T.-S. Kim
Department of Mechanical Engineering
Korea Advanced Institute of Science and Technology (KAIST)
291 Daehak-ro, Yuseong-gu, Daejeon 34141, Republic of Korea

H. Kim
R&D Center
DAVO C&M
215 Amsogogae-ro, Yan-gam myeon, Hwaseong-Si, Gyeonggi-do 18635,
Republic of Korea

 The ORCID identification number(s) for the author(s) of this article can be found under <https://doi.org/10.1002/admt.202100431>.

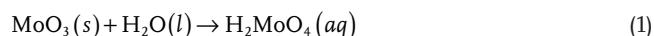
DOI: 10.1002/admt.202100431

and transferred to various substrates with different surface profiles. Several groups have delaminated TFTs from rigid substrates via the chemical etching of the sacrificial layer to develop flexible optoelectronic devices, field-effect transistor, and other devices.^[15–17] However, the chemical etching of the sacrificial layer is a time-consuming process that limits the manufacturing of large sized flexible devices.^[18,19] To overcome this drawback, extensive research has been conducted on the delamination of devices using a physical force. Furthermore, the successful fabrication of thin-film solar cells with flexible substrates has been realized by crack or water-assisted debonding.^[20,21]

It has been reported that the delamination of films by the debonding between two adjacent layers is accelerated under a corrosive environment.^[22] In this study, we utilized water-soluble molybdenum oxide^[23] as the exfoliation layer. This allowed the device to be delaminated from the substrate owing to the reaction with the H₂O in air at the crack of the interlayer region. The oxide TFTs were fabricated on a molybdenum oxide deposited on the glass substrate by the conventional process for fabricating display devices. The fabricated TFTs were subjected to post-annealing; subsequently, they were detached from the substrate using a physical force and transferred to the flexible, transparent 5 μm-thick PET substrates. Since the oxide TFTs were fabricated on a glass substrate, they could be processed at high temperatures. This facilitated the optimization of the electrical characteristics of the devices. The flexible and transparent devices were attached to the objects with complex curvilinear surfaces such as artificial leather, human skin, and contact lens. The ultra-thin devices retained their outstanding electrical performance in the bending state, despite the application of a high bending stress.

2. Results and Discussions

The deposition of a suitable exfoliation layer is necessary to delaminate the oxide TFTs from the rigid substrate. This study demonstrated the utilization of molybdenum trioxide (MoO₃) as the exfoliation layer because MoO₃ can react with water to form molybdic acid according to the following reaction:^[24]



Humid air acts as a corrosive environment for MoO₃ owing to the water solubility of MoO₃. This promotes the occurrence of debonding in humid air. The environment-assisted debonding reaction is also facilitated by the formation of an –OH terminated fracture according to Equation (1). MoO₃ exhibits a higher reactivity with water than that exhibited by other molybdenum oxides with different compositions. Therefore, an exfoliation layer comprising MoO₃ was deposited by reactive sputtering with a molybdenum (Mo) target in this study. To regulate the chemical composition, the molybdenum oxide layer was separately deposited using a reactive gas mixture with different ratios of argon (Ar) and oxygen (O₂).

X-ray photoelectron spectroscopy (XPS) was performed to determine the chemical composition of the Mo peaks for the molybdenum oxide films that were deposited with various

reactive gas ratios. The results of the analysis are presented in **Figure 1a**. When molybdenum oxide was initially deposited with a reactive gas ratio of 6:4 (Ar:O₂), the XPS results showed a dominant Mo⁴⁺ peak that corresponded to the composition of molybdenum dioxide (MoO₂). Therefore, this reactive gas ratio was not suitable for the deposition of the exfoliation layer. When molybdenum oxides were deposited with a reactive gas ratio of 5:5 and 3:7 (Ar:O₂), the XPS results showed the presence of a dominant Mo⁶⁺ peak that corresponded to the composition of MoO₃. A scrutiny of the Mo peaks revealed the presence of a relatively high concentration of Mo⁵⁺ in the film that was deposited with a reactive gas ratio of 5:5 (Ar:O₂). Therefore, a relatively low portion of oxygen in molybdenum oxide was obtained from the MoO_x film that was deposited with the reactive gas ratio of 5:5 (Ar:O₂). The atomic concentrations (in percentage) of molybdenum and oxygen in the deposited molybdenum oxide films were determined from the area of the Mo 3d and the O 1s peak, respectively, and the results are presented in Figure S1, Supporting Information. The molybdenum oxide film that was deposited with a reactive gas ratio of 6:4 (Ar:O₂) contained a relatively low amount of oxygen. The atomic concentration of oxygen in the molybdenum oxide film increased with the increase in the proportion of oxygen in the reactive gas. The composition of the molybdenum oxide film that was deposited with a reactive gas ratio of 3:7 (Ar:O₂) was approximately identical to that of MoO₃.

The reactivity of the deposited molybdenum oxide with H₂O was investigated by determining the etching rate in water. The etching rates in water for the molybdenum oxide thin films that were deposited with a reactive gas ratio of 5:5 and 3:7 (Ar:O₂) were compared. The analysis revealed that the etching rate in water varied significantly depending on the composition of molybdenum oxide (Figure 1b). The molybdenum oxide film deposited with a reactive gas ratio of 3:7 (Ar:O₂) exhibited a higher solubility in water (26.2 nm s^{−1}) as compared to that of the film deposited with a reactive gas ratio of 5:5 (Ar:O₂) (1.4 nm s^{−1}). Furthermore, a research group led by Moon indicated that the water solubility of amorphous MoO₃ was higher than that of the crystalline MoO₃ owing to the intrinsic structural disorder and the presence of defects.^[23] The absence of noticeable sharp peaks in the X-ray diffraction (XRD) pattern (Figure 1c) confirmed the amorphous nature of the molybdenum oxide film deposited by reactive sputtering. As a result, it is reasonable to assume that the molybdenum oxide film deposited by reactive sputtering reported here is highly soluble in water. Therefore, the molybdenum oxide film deposited with a reactive gas ratio of 3:7 (Ar:O₂) eased the delamination by reacting with the H₂O in air, thereby inducing the environment-assisted debonding.

The surface profile of the film was closely related to the adhesion energy.^[25] The surface area of the films increased with the increase in the roughness of the films. As a result, the contact area between the layers increased, resulting in increased adhesion energy. The surface profile of the molybdenum oxide layer was investigated by atomic force microscopy (AFM) and is presented in Figure 1d. The image revealed a smooth surface with a root mean square roughness of 0.24 nm. Therefore, the molybdenum oxide layer was suitable for use as the exfoliation layer. In here, we adopted the 100 nm thick of molybdenum oxide as the exfoliation layer.

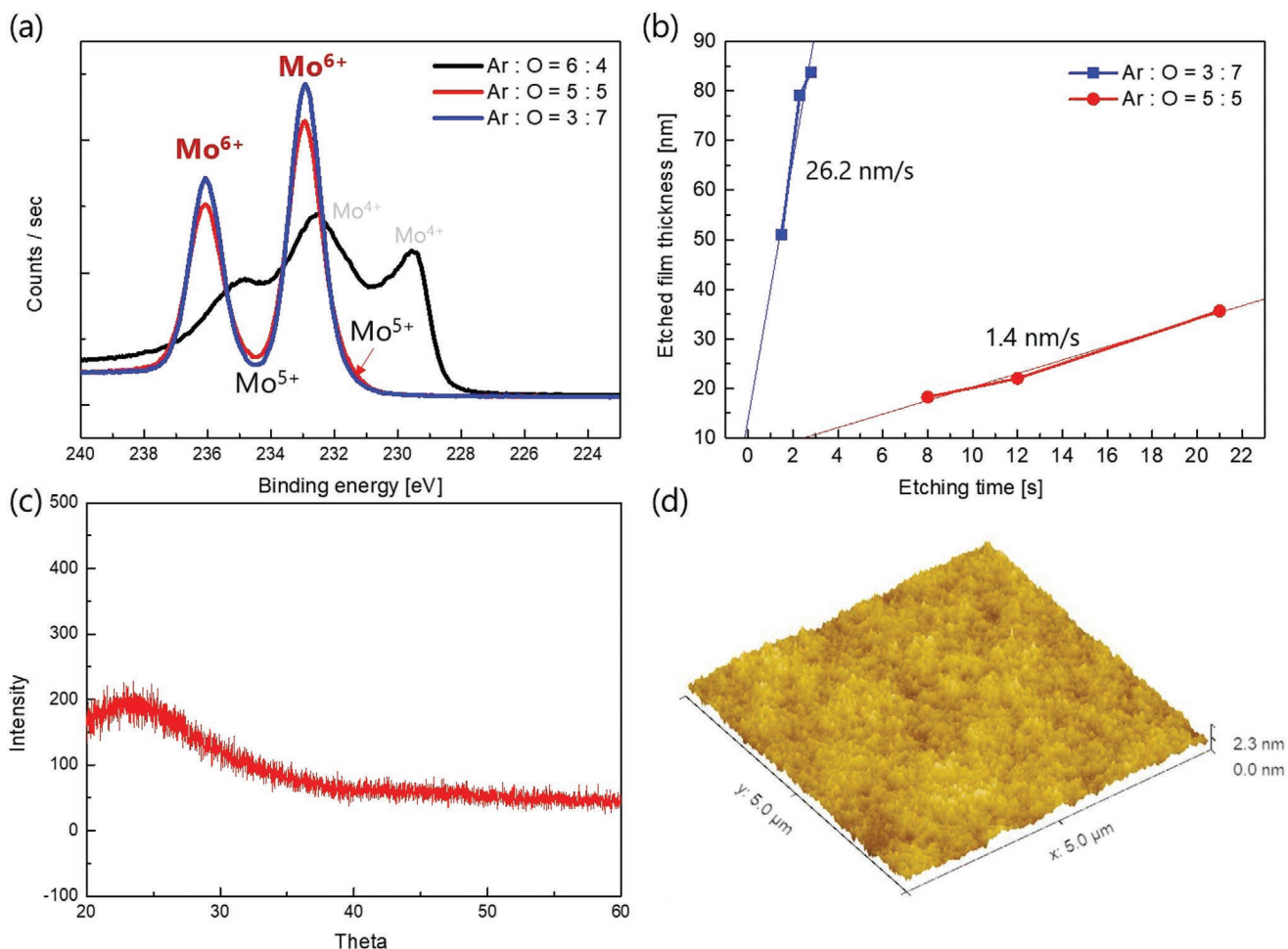


Figure 1. a) XPS Mo 3d peaks of the molybdenum oxide layers that are deposited with various reactive gas ratios. b) The thicknesses of the molybdenum oxide etched in water depending on the reactive gas ratios. c) XRD pattern for the molybdenum oxide film on the glass substrate. d) Surface profile of the molybdenum oxide layer, as determined by AFM.

Figure 2a shows a schematic of the process of transferring the oxide TFT from the rigid glass substrate to the flexible and transparent PET substrate. Prior to the fabrication of the oxide TFTs, the molybdenum oxide layer was deposited on the glass substrate by reactive sputtering to form the exfoliation layer (thickness = 100 nm). Subsequently, barrier layers comprising 180 nm-thick silicon nitride (Si_3N_4) as the bottom layer and 20 nm-thick aluminum oxide (Al_2O_3) as the top layer were deposited to prevent the contaminant-induced deterioration in the electrical characteristics of the TFTs. The oxide TFTs were fabricated on the barrier layers using a vacuum-based process at a temperature below 350 °C. The processes for the fabrication of the oxide TFTs are illustrated in Figure S2, Supporting Information. The carrier film was spin casted on the samples and the oxide TFTs were delaminated from the rigid substrate by applying a physical force after the completion of the fabrication and post-annealing. The layers of molybdenum oxide and the inorganic barrier (Si_3N_4) were easily separated at the interface by an applied physical force. The detached device, including the adhesive layer, was transferred to the 5 μm-thick PET substrate, and the carrier film was removed to open the electrode pad of the TFT device. Figure 2b shows the transferred oxide TFT on the 5 μm-thick PET substrate. The

optical microscopy (OM) images of the flexible devices (Figure 2c) showed that the oxide TFTs were delaminated and transferred to the PET substrate without any noticeable damage generated by cracking and wrinkling. The 5 μm-thick flexible devices uniformly covered and attachment to objects with simple surface profiles such as glasses (Figure 2d) and contact lenses (Figure 2e), objects with complex surface profiles such as clothes (Figure 2f), and biological tissues such as human skin (Figure 2g) without wrinkling or the presence of delaminated regions when visually identified. When the fabricated flexible devices in this study were attached to different objects, they were not easily detected owing to their ultrathin and transparent nature.

To understand the mechanism of the easy delamination of the oxide TFTs, the interface at the delamination region was investigated by high-resolution transmission electron microscopy (HRTEM). The debonding could occur at the following interfaces: 1) between the barrier layer and the molybdenum oxide layer, 2) inside the molybdenum oxide layer, and 3) between the molybdenum oxide layer and the glass substrate. The HRTEM image of the boundary between the delaminated region and the remaining area of the device was investigated to confirm the delamination surface. The analysis of the HRTEM

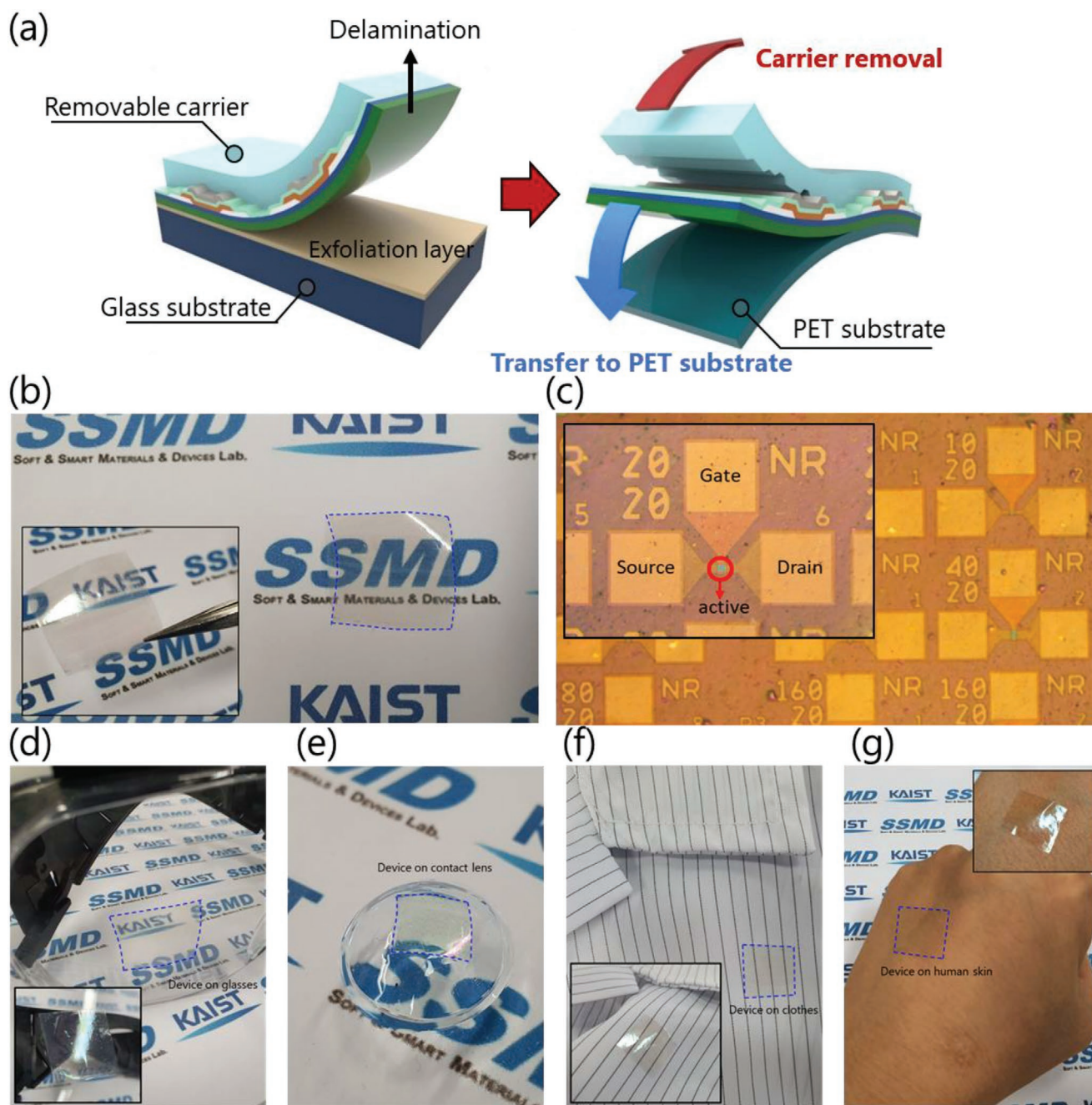


Figure 2. a) Schematic illustration of the process of delamination and transfer. b) The transparent and flexible oxide TFT that is delaminated from the rigid substrate and transferred to the 5 μm -thick PET substrate. The inset shows the picking of the flexible devices with tweezers. c) The magnified OM image of the oxide TFT on the PET substrate. The inset indicates the magnified single-oxide TFT. A photograph of the flexible device that is attached to the d) curved glass, e) contact lens, f) chest region of clothes, and g) back of the hand. The insets in each figure show the flexible devices reflecting the lamp light.

image of the delaminated region (Figure 3a) indicated the removal of the oxide TFT with the silicon nitride barrier layer during delamination; however, the molybdenum oxide layer remained intact. Therefore, it was confirmed that delamination occurred at the interface between the silicon nitride barrier layer and the molybdenum oxide layer. Furthermore, the elemental mapping of molybdenum and silicon by energy-dispersive spectrometry revealed the absence of silicon at the

delaminated region (Figure S3, Supporting Information). Therefore, the oxide TFTs were delaminated from the molybdenum oxide layer without leaving any residue.

The HRTEM image confirmed the occurrence of debonding between the silicon nitride and the molybdenum oxide layers. Therefore, the adhesion energy between the two layers was measured by the double cantilever beam method. The schematic of the double cantilever beam (DCB) specimen is presented in

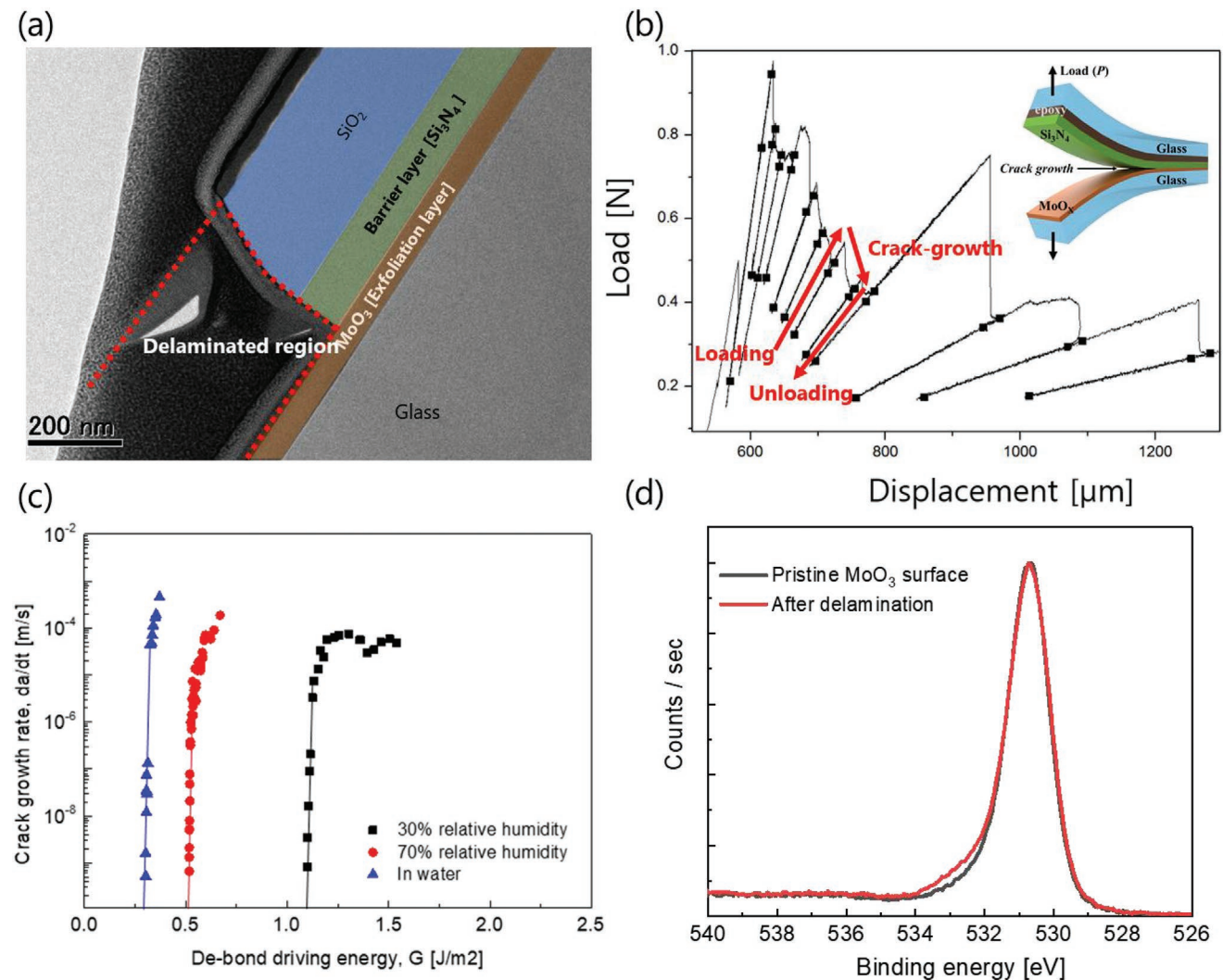


Figure 3. a) Cross-sectional TEM image of the oxide TFTs that are fabricated on the molybdenum oxide layer, including the delaminated region. b) The measured applied load as a function of the displacement during the repeating loading and unloading at a constant displacement rate. c) The crack growth behavior at the interface between the molybdenum oxide and silicon nitride layers in air at 30% RH and 70% RH and in water. d) XPS O1s peaks of the molybdenum oxide surface in the pristine state and after the delamination of silicon nitride from molybdenum oxide.

the inset of Figure 3b. The DCB specimens were loaded and unloaded with a constant loading speed of $0.2 \mu\text{m s}^{-1}$, and the applied force and the displacement were measured simultaneously. The critical load at which delamination starts to occur was $\approx 0.98 \text{ N}$ as shown in Figure 3b, and it was confirmed that delamination occurred even with little force. The applied load (P) and displacement (δ) were utilized to calculate the crack length (a) and the fracture energy (G_c) using the following equations:

$$a = \left(\frac{CE'Bh^3}{8} \right)^{1/3} - 0.64h \quad (2)$$

$$G_c = \frac{12P_c^2 a^2}{E'B^2h^3} \left(1 + 0.64 \frac{h}{a} \right)^2 \quad (3)$$

where C is the elastic compliance of specimen that can be obtained from $d\delta/dP$, P_c is the critical load at which the crack

starts to grow, and E' is the plane-strain modulus of the beam (glass). B and h are the width and half-height, respectively, of the specimens. The adhesion energy between the silicon nitride and molybdenum oxide layers was measured in lab air and determined to be $0.81 \pm 0.08 \text{ J m}^{-2}$ that was similar to the adhesion energy between Cu and graphene ($0.72 \pm 0.07 \text{ J m}^{-2}$). It is well known that the layers of Cu and graphene can be easily delaminated.^[26] Since the adhesion between the barrier layer of the oxide TFTs and the molybdenum oxide film was weak, the TFTs were easily delaminated from the rigid substrate without leaving any residue. In addition, it is expected that the peel-off method can be implemented in a large area, because the extracted adhesion energy of a large size such as 6 G ($1500 \times 1850 \text{ mm}$) is small as 2.24 J.

The delamination of the oxide TFTs from the molybdenum oxide layer was ascribed to the environment-assisted subcritical debonding. This principle was validated by measuring the crack growth rates at the interface between the silicon nitride and molybdenum oxide layers under various humidity

conditions in air and in water. Figure 3c shows the variation in the measured crack growth rates with the applied debond driving energy in air with a relative humidity (RH) of 30 and 70% and in water at a fixed temperature, 30 °C. The relative position of the curves was highly dependent on the RH and the environment. The curve corresponding to the debonding in water exhibited a low threshold debond driving energy (G_{th}) of $\approx 0.30 \text{ J m}^{-2}$. The G_{th} in air at an RH of 30% and 70% was 1.09 and 0.51 J m^{-2} , respectively, showing clear decreasing trend of the G_{th} with increasing relative humidity. The significant variation in the G_{th} with the relative humidity indicated that the interface between the silicon nitride and molybdenum oxide layers was susceptible to interactions with the water in air.^[27] Therefore, the water content in the environment affected the debonding behavior between the silicon nitride and molybdenum oxide layers. The high reactivity of molybdenum oxide with H_2O promoted the chemical reaction at the crack region. This facilitated the debonding and lowered the adhesive strength between the layers. Therefore, the easy delamination of the TFTs was attributed to the reaction with H_2O at the crack tip.

The peaks in the XPS spectra of the delaminated surface were analyzed to confirm the formation of the $-\text{OH}$ terminated fracture surface owing to the environment-assisted debonding. Figure 3d shows the O1s peak for the molybdenum oxide surface before and after the delamination of the silicon nitride layer. The XPS O1s spectra comprised peaks that corresponded to the oxygen vacancies, the $\text{M}-\text{O}$ bonds, and the $\text{O}-\text{C}$ or $\text{O}-\text{H}$ bonds. The binding energies of the peaks corresponding to the oxygen vacancy ($\approx 531.8 \text{ eV}$) and $-\text{OH}$ ($\approx 532.8 \text{ eV}$) were higher than that of the peaks corresponding to the $\text{M}-\text{O}$ bond.^[28,29] There was a significant increase in the binding energy shoulder after the delamination of the silicon nitride layer from the molybdenum oxide layer. This was attributed to the generation of $-\text{OH}$ at the molybdenum oxide surface after delamination. The deconvolution results of the O1s peaks and the calculated concentrations of the bonding states are presented in Figure S4 and Table S1, Supporting Information, respectively. It was inferred that structural defects such as dangling bonds were generated at the interlayer during the delamination of the silicon nitride layer by the application of a physical force; in addition, $-\text{OH}$ was also generated by the reaction with the H_2O in air. Therefore, the molybdenum oxide layer and the inorganic layer were easily delaminated owing to the generation of the $-\text{OH}$ terminated fracture.

The characteristics of the oxide TFTs are affected significantly by the mechanical force or deformation induced during the delamination from a rigid substrate. Therefore, it is important to modify the thickness of the carrier film to place the neutral plane close to the brittle device. A schematic of the mechanism of delamination and the position of the neutral plane is presented in Figure 4a. A group of researchers led by Rogers proposed that the position of the neutral plane is determined by the following equation:^[30]

$$h_{\text{neutral}} = \frac{\sum_{i=1}^N \bar{E}_i h_i \left(\sum_{j=1}^i h_j - \frac{h_i}{2} \right)}{\sum_{i=1}^N \bar{E}_i h_i} \quad (4)$$

where \bar{E}_i and h_i are the effective Young's modulus and the thickness, respectively, of the i th layer. The effective Young's modulus was calculated using the following equation:

$$\bar{E}_i = \frac{E_i}{1 - \nu_i^2} \quad (5)$$

where E_i and ν_i are the Young's modulus and the Poisson's ratio, respectively, of the i th layer. The elastic properties and the layer thicknesses for the system of the flexible oxide TFTs were as follows: (1) $E_{\text{carrier}} = 20 \text{ GPa}$, $\nu_{\text{carrier}} = 0.44$, and $h_{\text{carrier}} = \text{variable}$, (2) $E_{\text{ITO}} = 116 \text{ GPa}$, $\nu_{\text{ITO}} = 0.35$, and $h_{\text{ITO}} = 0.15 \text{ }\mu\text{m}$, (3) $E_{\text{AlOx}} = 370 \text{ GPa}$, $\nu_{\text{AlOx}} = 0.22$, and $h_{\text{AlOx}} = 0.02 \text{ }\mu\text{m}$, (4) $E_{\text{IGZO}} = 137 \text{ GPa}$, $\nu_{\text{IGZO}} = 0.36$, and $h_{\text{IGZO}} = 0.02 \text{ }\mu\text{m}$, (5) same as that of the third layer, and (6) $E_{\text{SiNx}} = 166 \text{ GPa}$, $\nu_{\text{SiNx}} = 0.23$, and $h_{\text{SiNx}} = 0.3 \text{ }\mu\text{m}$. The results of the calculation indicated that the neutral plane moved in the device direction with the decrease in the thickness of the carrier film.

The electrical characteristics of the oxide TFTs were dependent on the property of the channel. Therefore, the applied strain at the interface between the active layer and the gate insulator was determined based on the thickness of the carrier film and the bending radius. The distance between the neutral plane and the channel region is indicated as x in Figure 4a. The applied strain was calculated by following equation:^[31]

$$\varepsilon = \frac{x}{R} \quad (6)$$

where ε is the applied strain at the channel region, and R is bending radius during delamination. The strain at the device region during the delamination was determined based on the thickness of the carrier film (Figure 4b). The graph indicated that the decrease in the thickness of the carrier film causes lower strain in the channel region of devices.

The changes in the transfer characteristics of the devices before and after the delamination were investigated based on the thickness of the carrier film. Figure 4c,d presents the variation in the transfer characteristics of the TFTs for a thick and thin carrier film, respectively, before and after delamination. The figures showed that the transfer curve for the thick carrier film shifted to the negative direction after the delamination. In previous studies, when the oxide TFTs are subjected to physical stress and strain, it has been demonstrated through technology computer-aided design (TCAD) analysis that the oxygen vacancies (V_o) are generated due to the break of bonding between metal and oxide, causing an increase of donor-like V_o^+ / V_o^{2+} states.^[32,33] When the thick carrier film was utilized for the delamination of the oxide TFTs, numerous oxygen vacancies were generated owing to the high applied strain. This resulted in the negative shift of the transfer curve. When the thin carrier film was utilized for the delamination of the oxide TFTs, a low strain was induced in the channel region. This resulted in no significant changes in the transfer characteristics after the delamination (Figure 4d). The separation between the neutral plane and the device decreased with the decrease in the thickness of the carrier film. This resulted in the lowering of the applied strain at the channel region. Therefore, the use of the thin carrier film induced no significant changes in the electrical characteristics of the TFTs after delamination.

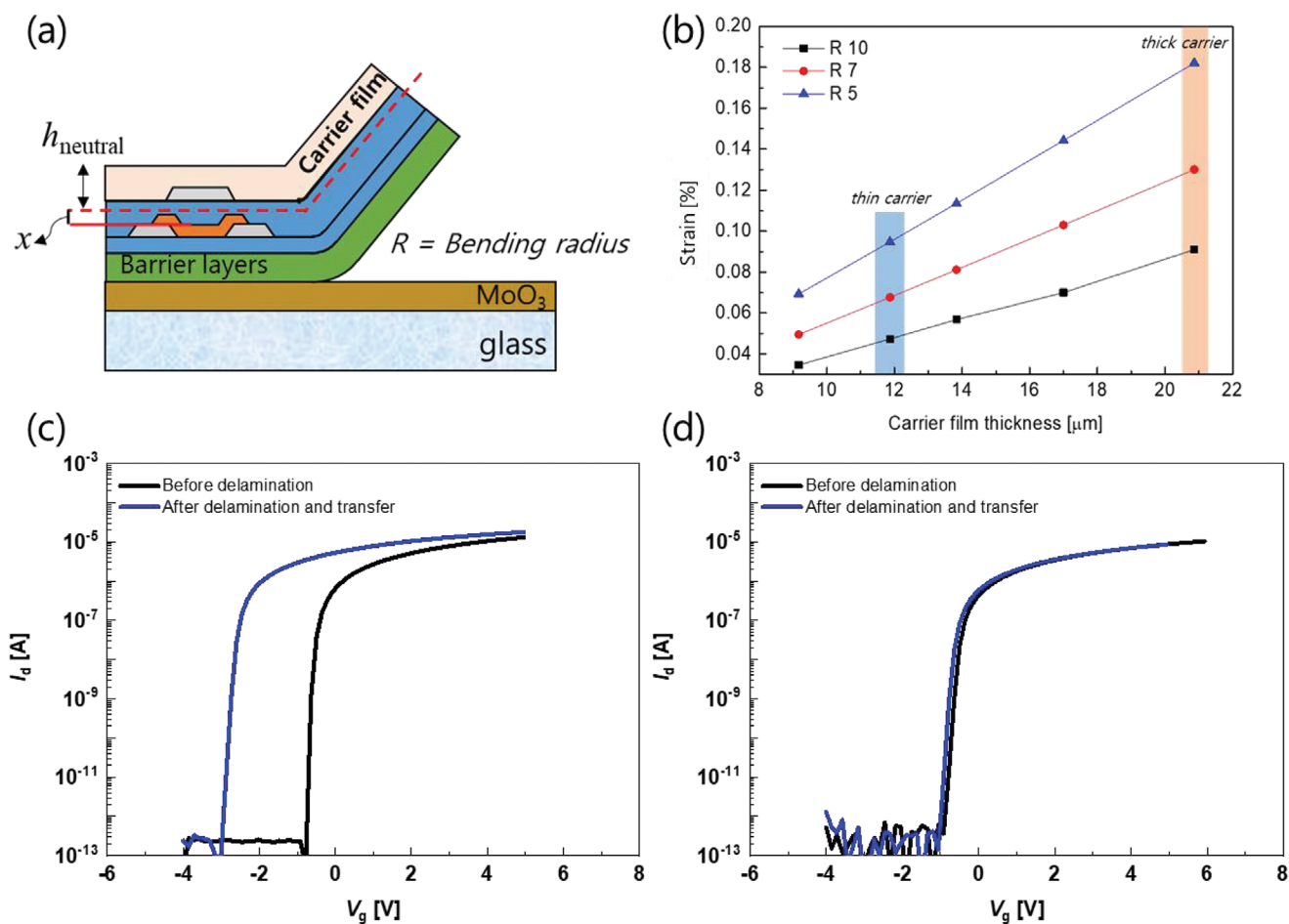


Figure 4. a) Schematic illustration of the delamination of the oxide TFTs and the position of the neutral plane. b) The variation in the applied strain at the channel region of the oxide TFTs with the carrier film thickness during the delamination, for various bending radii. The variation in the transfer characteristics of the devices before the delamination and after the delamination and subsequent transfer to the PET substrate with the application of c) thick and d) thin carrier films for delamination.

The optical and electrical characteristics of the flexible oxide TFTs after the delamination and transfer are presented in Figure 5. The optical transmittance of the PET substrate and that of the oxide TFT on the PET substrate were compared by ultraviolet-visible (UV-vis) spectroscopy to investigate the transparency of the transferred devices. The optical transparency of each sample was measured within a wavelength range of 350–800 nm. The UV-vis transmittance spectra of the PET and the flexible devices are shown in Figure 5a. The transmittance of the PET substrate was 88%.^[34–36] The flexible oxide TFTs on the PET substrate exhibited an average transmittance of greater than 82% in the visible light region (400–700 nm). The inset of Figure 5a shows that the emblem behind the TFT was clearly visible. This indicated the high transparency of the fabricated TFTs.

The electrical parameters of the transparent and flexible devices were determined from the transfer characteristics of the sixteen individual oxides TFTs on the PET substrate. Figure 5b shows the 95% confidence interval for the mean values of the turn-on voltage (V_{on}), field-effect mobility, and subthreshold swing (S.S). The flexible oxide TFTs were reasonably uniform after the delamination and the transfer to the PET substrate. Figure S5, Supporting Information shows the histogram

distribution and the Gaussian fitting curves of the V_{on} , field-effect mobility, and S.S. The oxide TFTs on the PET substrate exhibited an average V_{on} of -1.02 V and a high mobility of 29.8 cm^2 V^{-1} s^{-1} . The low S.S of 0.088 V dec^{-1} for the flexible and transparent oxide TFTs indicated the existence of a few trap sites at the interface between the active layer and the gate insulator.^[37–39] The TFTs also exhibited highly saturated optimal output characteristics and no contact issues (Figure S6, Supporting Information).

When TFTs are operated as the backplane of displays, they must be stressed under a positive and negative gate bias.^[40] Furthermore, the high transparency of oxide TFTs induces the exposure to stress under light illumination.^[41] The application of a negative gate bias and illumination to the devices induced a negative V_{on} shift. The flexible and transparent oxide TFTs were subjected to a positive bias stress (PBS), negative bias stress (NBS), positive bias illumination stress (PBIS), and negative bias illumination stress (NBIS). The resulting transfer curves were obtained to determine the electrical stability of the TFTs. A positive and negative gate bias stress of 2 V (1 MV cm^{-1}) and -2 V (-1 MV cm^{-1}), respectively, were applied. There were no significant changes in the transfer characteristics by the application of the PBS (Figure 5c) and NBS (Figure 5d) for 10 000 s.

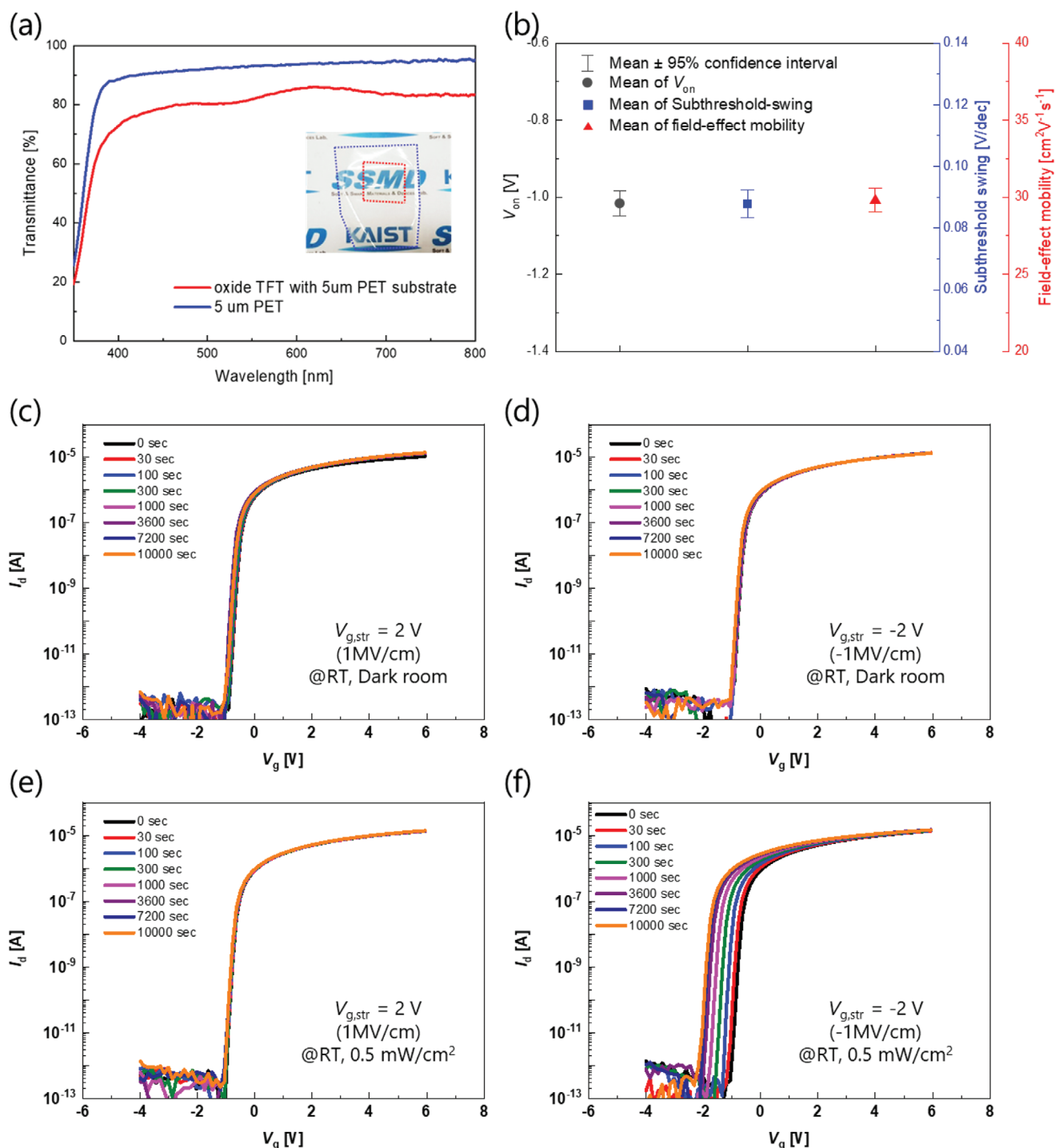


Figure 5. a) The UV–vis transmittance spectra for the flexible device and the PET substrate. b) The mean of the V_{on} , S.S., and field-effect mobility for the 16 oxide TFTs on the PET substrate, with a 95% confidence interval. The variation in the transfer curves of the flexible oxide TFTs under the c) PBS, d) NBS, e) PBIS, and f) NBIS for 10 000 s.

The fabrication and annealing of the TFTs without any temperature limitations facilitated the generation of high-quality interfaces and composite layers. Therefore, the TFTs exhibited high electrical stability.^[42,43] Figure 5e,f show the electrical stability of the oxide TFTs under the PBIS and NBIS, respectively. The samples were subjected to an illumination of 0.5 mW cm^{-2}

under a gate bias stress. When the TFTs were subjected to the PBIS, there were negligible changes in the transfer characteristics. Meanwhile the exposure of TFTs to the NBIS resulted in the transfer curve shift to the negative direction (1.09 V). The ionized V_o was generated from the deep states of the oxide semiconductors and trapped at the gate insulator to induce

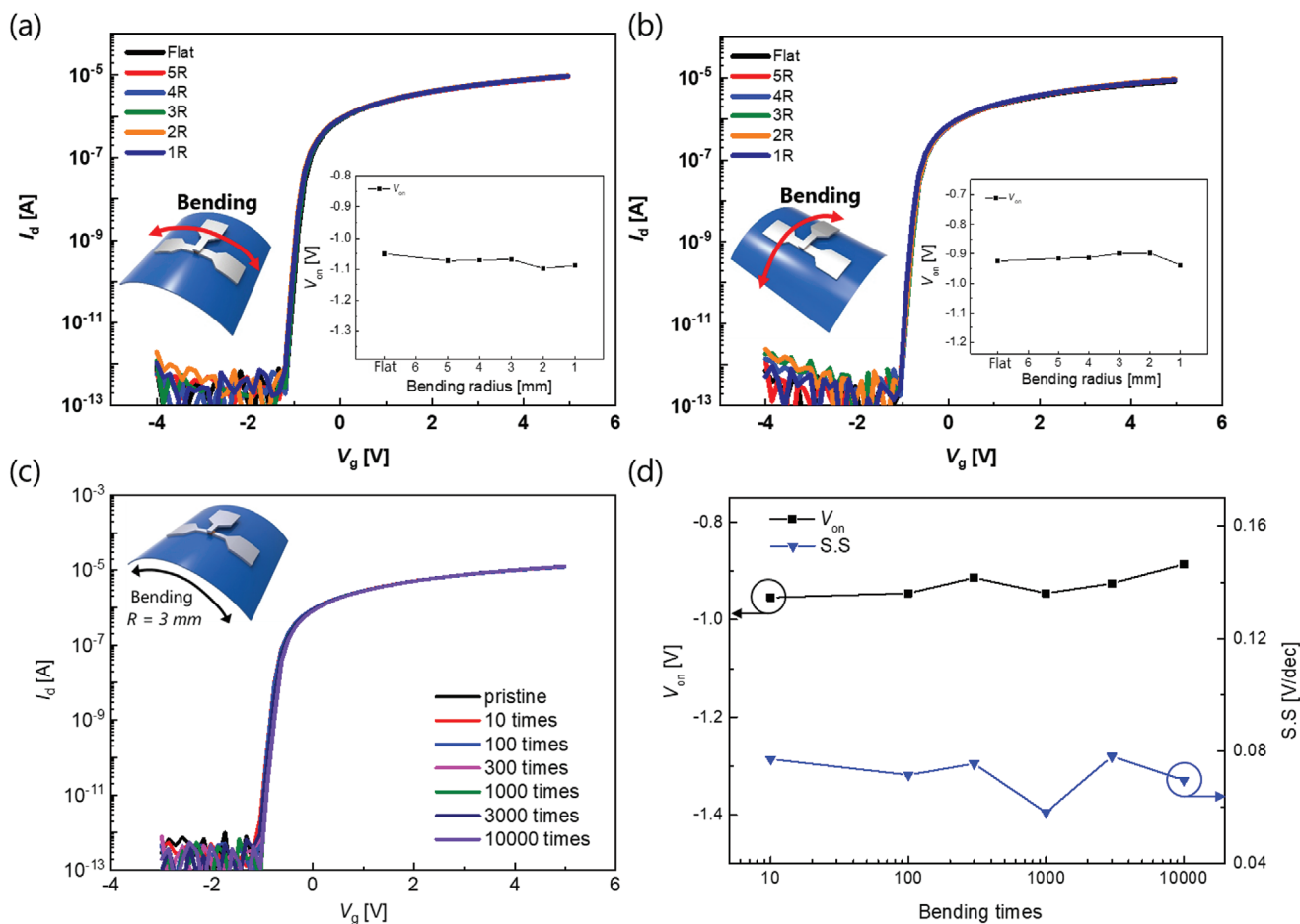


Figure 6. The transfer characteristics of the flexible and transparent oxide TFTs on the curved metal mold with various curvatures, where the bending axis is a) perpendicular and b) parallel to the channel. The insets indicate the variation in the V_{on} . c) The transfer curves and d) the variations in the V_{on} and S.S. of the flexible device after the repetitive bending over several cycles with a bending radius of 3 mm.

the V_{on} shift to the negative direction under the illumination stress. Furthermore, the gate insulator, which contained a high concentration of OH, induced a severe deterioration in the stability of the devices under the NBIS. The diffusion of H, from the OH in the gate insulator, into the active layer during the thermal annealing of the devices resulted in the formation of a non-bridging oxygen hole center (NBOHC) at the middle gap of the gate insulator. The holes or the ionized V_o were trapped in this NBOHC, thereby inducing the negative shift of the transfer curve.^[44,45] The use of aluminum oxide that was fabricated by thermal atomic layer deposition (ALD) as the gate insulator in this study facilitated the realization of highly stable devices under a positive gate bias stress. It has been demonstrated that plasma-based techniques such as plasma-enhanced ALD for the formation of gate insulators generate electron trap sites.^[46,47] The shifting of the transfer curves under the NBIS was attributed to the high concentration of hydrogen in the aluminum oxide that was fabricated by thermal ALD. The stability of the devices under the NBIS, however, can be improved by optimizing the properties of the gate insulator.

The mechanical properties of the flexible and transparent oxide TFTs were also investigated in this study. First, the transfer characteristics of the flexible and transparent oxide

TFTs were analyzed in the bending state with different bending radii and directions. Figure S7, Supporting Information shows the photographs of the system for the measurement of the electrical characteristics of the flexible oxide TFTs in the bending state with a bending radius of 1 mm. **Figure 6a,b** show the transfer curves of the bent oxide TFTs for various bending radii with the bending axis perpendicular and parallel to, respectively, the channel direction. The flexible oxide TFTs exhibited typical transfer characteristics in the bending state without any significant changes in their electrical performance, regardless of the bending radius and direction. The variation in the V_{on} of the flexible oxide TFTs with the bending radius is shown in the insets of Figure 6a,b. When the bending axis was perpendicular and parallel to the channel direction, with a bending radius of 1 mm, the V_{on} shifted by only -0.04 and -0.01 V, respectively, for the curved metal mold. Furthermore, the ultrathin nature of the flexible substrate and the oxide TFTs facilitated the lowering of the strain that was applied to the devices in the bending state, even at low bending radii.^[18,48,49]

The mechanical durability of the oxide TFTs on the PET substrate was determined by measuring the change in the transfer characteristics over several bending cycles. The schematic diagram of the bent flexible and transparent oxide TFTs

in the inset of Figure 6c indicates that the device was bent in a direction that was perpendicular to the channel direction with a bending radius of 3 mm. Figure 6c,d show the variation in the transfer characteristics of the devices and the measured electrical parameters, respectively, during the repeated bending over 10 000 cycles. The V_{on} and S.S exhibited minor changes by 0.03 V and 0.001 V dec^{-1} , respectively, during the repeated bending over 10 000 cycles. Therefore, the flexible and transparent oxide TFTs that were fabricated by delamination and transfer exhibited a high mechanical durability at a bending radius of 3 mm during the repeated bending over several cycles.

3. Conclusions

In this study, we demonstrated the fabrication of ultrathin flexible and transparent oxide TFTs by the technique of delamination and transfer. The high-performance oxide TFTs were fabricated on a rigid substrate without temperature limitations and transferred to a 5 μm -thick PET substrate. The devices exhibited optimal coverage on and attachment to various objects with complex surface profiles such as contact lens, clothes, and human skin. The results of the DCB test confirmed the low adhesion energy between the inorganic layer and the molybdenum oxide layer. The analysis of the crack growth rates under various humidity conditions confirmed that the delamination was facilitated by the reaction with H_2O at the interlayer crack tip. The oxide TFTs on the PET substrate exhibited a high optical transparency of greater than 81% and a satisfactory electrical performance with a high mobility of 37 $\text{cm}^2 \text{V}^{-1} \text{s}^{-1}$. The devices also exhibited a high electrical stability under gate bias and illumination stresses. The ultrathin flexible oxide TFTs possessed excellent mechanical properties; furthermore, they showed a high mechanical durability over 10 000 cycles of repeated bending with a bending radius of 3 mm. These thin film devices also showed reliable transfer characteristics in the bending state, regardless of the bending radius and direction. This study demonstrated that flexible oxide TFTs could be fabricated without temperature limitations by delamination and transfer using a suitable exfoliation layer. Furthermore, it is expected that the devices transferred to the PET substrate could also be directly attached to various substrates. This flexibility was attributed to the ultrathin nature of the TFTs. The fabricated flexible oxide TFTs in this study could be potentially applied to the development of next-generation deformable displays such as multi-foldable, rollable, and stretchable displays owing to their outstanding optical, electrical, and mechanical properties.

4. Experimental Section

Fabrication of the Oxide TFT: The formation of the exfoliation layer involved the deposition of a 100 nm-thick layer of molybdenum oxide on a glass substrate by reactive sputtering with a molybdenum target. Subsequently, a 300 nm-thick layer of silicon nitride and a 20 nm-thick layer of aluminum oxide were deposited on the molybdenum oxide layer by plasma-enhanced chemical vapor deposition and plasma-enhanced ALD, respectively, at 300 °C. These layers acted as barriers and protected the oxide TFTs from contaminants. Indium-tin oxide

(ITO) was deposited and patterned as a source/drain electrode. A 20 nm-thick layer of Al-doped indium-tin-zinc oxide, which is a well-known oxide semiconductor with high mobility, was utilized as the active layer. Prior to the formation of the gate insulator, oxygen plasma treatment was conducted on the active layer under 200 W of power for 9 min to modulate the carrier density. The formation of the gate insulator involved the deposition of a 20 nm-thick layer of aluminum oxide by thermal ALD at 200 °C. ITO was deposited as the gate electrode. The fabricated TFTs were subjected to thermal annealing at 300 °C under a vacuum to optimize their electrical characteristics by curing the defects.

Delamination and Transfer of the Oxide TFT: The carrier film was formed by the spin casting of polyvinyl alcohol (PVA) on the fabricated and annealed devices. The oxide TFTs were delaminated from the rigid substrate with the application of a physical force (by hand) to the carrier film; subsequently, the devices were placed on the carrier film. The oxide TFTs on the carrier film were transferred to a 5 μm -thick flexible and transparent PET substrate with an adhesive layer. Subsequently, since the PVA carrier film was soluble in water, the carrier film was removed by rinsing with H_2O to open the electrode pad and measure the electrical performance.

Fabrication of the DCB Specimen: The DCB specimens were fabricated by the deposition of a 100 nm-thick layer of molybdenum oxide on a glass substrate by reactive sputtering with a reactive gas mixture of argon and oxygen ($\text{Ar}:\text{O}_2 = 7:3$). A 300 nm-thick layer of silicon nitride was deposited on the molybdenum oxide layer by PE-CVD at 300 °C. Thereafter, the glass was attached to the silicon nitride layer using epoxy (353ND) by curing at 120 °C for 2 h. The width and length of the DCB specimens were 8 and 50 mm, and the thickness of the glass substrate was 700 μm .

Supporting Information

Supporting Information is available from the Wiley Online Library or from the author.

Acknowledgements

This work was supported by the Wearable Platform Materials Technology Center (WMC) funded by a National Research Foundation of Korea (NRF) grant by the Korean Government (MSIT) (No. 2016R1A5A1009926). This work was also supported by the National Research Foundation of Korea (NRF) grant funded by the Korea government (MSIT) (2018R1A2A3075518).

Conflict of Interest

The authors declare no conflict of interest.

Data Availability Statement

Research data are not shared.

Keywords

attachable, delamination, thin films, transistors, ultrathin device

Received: April 12, 2021
Revised: May 24, 2021
Published online:

- [1] S.-I. Park, Y. Xiong, R.-H. Kim, P. Elvikis, M. Meitl, D.-H. Kim, J. Wu, J. Yoon, C.-J. Yu, Z. Liu, Y. Huang, K. Hwang, P. Ferreira, X. Li, K. Choquette, J. A. Rogers, *Science* **2009**, 325, 977.
- [2] J. A. Rogers, Z. Bao, K. Baldwin, A. Dodabalapur, B. Crone, V. R. Raju, V. Kuck, H. Katz, K. Amundson, J. Ewing, P. Drzaic, *Proc. Natl. Acad. Sci. U. S. A.* **2001**, 98, 4835.
- [3] A. Nathan, A. Ahnood, M. T. Cole, S. Lee, Y. Suzuki, P. Hiralal, F. Bonaccorso, T. Hasan, L. Garcia-Gancedo, A. Dyadyusha, S. Haque, P. Andrew, S. Hofmann, J. Moultrie, D. Chu, A. J. Flewitt, A. C. Ferrari, M. J. Kelly, J. Robertson, G. A. J. Amaratunga, W. I. Milne, *Proc. IEEE* **2012**, 100, 1486.
- [4] H.-H. Hsieh, H.-H. Lu, H.-C. Ting, C.-S. Chuang, C.-Y. Chen, Y. Lin, *J. Inf. Disp.* **2010**, 11, 160.
- [5] T. Wu, C.-W. Sher, Y. Lin, C.-F. Lee, S. Liang, Y. Lu, S.-W. H. Chen, W. Guo, H.-C. Kuo, Z. Chen, *Appl. Sci.* **2018**, 8, 1557.
- [6] J.-Y. Kwon, D.-J. Lee, K.-B. Kim, *Electron. Mater. Lett.* **2011**, 7, 1.
- [7] J. S. Park, W.-J. Maeng, H.-S. Kim, J.-S. Park, *Thin Solid Films* **2012**, 520, 1679.
- [8] K. Nomura, H. Ohta, A. Takagi, T. Kamiya, M. Hirano, H. Hosono, *Nature* **2004**, 432, 488.
- [9] Z. Zheng, Y. Zeng, R. Yao, Z. Fang, H. Zhang, S. Hu, X. Li, H. Ning, J. Peng, W. Xie, X. Lu, *J. Mater. Chem. C* **2017**, 5, 7043.
- [10] Y. Jung, T. Jun, A. Kim, K. Song, T. H. Yeo, J. Moon, *J. Mater. Chem.* **2011**, 21, 11879.
- [11] M. C. Mcalpine, H. Ahmad, D. Wang, J. R. Heath, *Nat. Mater.* **2007**, 6, 379.
- [12] R. Yao, Z. Zheng, Z. Fang, H. Zhang, X. Zhang, H. N. , L. Wang, J. Peng, W. Xie, X. Lu, *J. Mater. Chem. C* **2018**, 6, 2522.
- [13] L. Zhang, W. Xiao, W. Wu, B. Liu, *Appl. Sci.* **2019**, 9, 773.
- [14] X. Li, M. M. Billah, M. Mativenga, D. Geng, Y.-H. Kim, T.-W. Kim, Y.-G. Seol, J. Jang, *IEEE Electron Device Lett.* **2015**, 36, 811.
- [15] J. Yoon, S. Jo, I. S. Chun, I. Jung, H.-S. Kim, M. Meitl, E. Menard, X. Li, J. J. Coleman, U. Paik, J. A. Rogers, *Nature* **2010**, 465, 329.
- [16] D.-H. Kim, J. Viventi, J. J. Amsden, J. Xiao, L. Vigeland, Y.-S. Kim, J. A. Blanco, B. Panilaitis, E. S. Frechette, D. Contreras, D. L. Kaplan, F. G. Omentto, Y. Huang, K.-C. Hwang, M. R. Zakin, B. Litt, J. A. Rogers, *Nat. Mater.* **2010**, 9, 511.
- [17] Y. Yang, Y. Hwang, H. A. Cho, J.-H. Song, S.-J. Park, J. A. Rogers, H. C. Ko, *Small* **2011**, 7, 484.
- [18] G. A. Salvatore, N. Munzenrieder, T. Kinkeldei, L. Petti, C. Zysset, I. Strelbel, L. Buthe, G. Troster, *Nat. Commun.* **2014**, 5, 2982.
- [19] C.-W. Cheng, K.-T. Shiu, N. Li, S.-J. Han, L. Shi, D. K. Sadana, *Nat. Commun.* **2013**, 4, 1.
- [20] C. H. Lee, J.-H. Kim, C. Zou, I. S. Cho, J. M. Weisse, W. Nemeth, Q. Wang, A. C. T. van Duin, T.-S. Kim, X. Zheng, *Sci. Rep.* **2013**, 3, 1.
- [21] C. H. Lee, D. R. Kim, I. S. Cho, N. William, Q. Wang, X. Zheng, *Sci. Rep.* **2012**, 2, 1000.
- [22] J. C. Card, R. M. Cannon, E. Saiz, A. P. Tomsia, R. O. Ritchie, *J. Appl. Phys.* **2007**, 102, 053516.
- [23] J.-Y. Moon, S.-I. Kim, S.-K. Son, S.-G. Kang, J.-Y. Lim, D. K. Lee, B. Ahn, D. Whang, H. K. Yu, J.-H. Lee, *Adv. Mater. Interfaces* **2019**, 6, 1970087.
- [24] T. P. Dadze, G. A. Kashirtseva, M. P. Novikov, A. V. Plyasunov, *Fluid Phase Equilib.* **2017**, 440, 64.
- [25] S. H. Lee, R. J. Stewart, H. Park, S. Goyal, V. Botu, H. Kim, K. Min, E. Cho, A. R. Rammohan, J. C. Mauro, *J. Phys. Chem. C* **2017**, 121, 24648.
- [26] T. Yoon, W. C. Shin, T. Y. Kim, J. H. Mun, T.-S. Kim, B. J. Cho, *Nano Lett.* **2012**, 12, 1448.
- [27] M. Giachino, F. Paredes, N. Ananthakrishnan, S. M. Liff, R. H. Dauskardt, *IEEE Int. Interconnect Technol. Conf.* **2014**, 4, 359.
- [28] S. Y. Turishchev, O. A. Chuvankova, E. V. Parinova, D. A. Koyuda, R. G. Chumakov, M. Presselt, A. Schleusener, V. Sivakov, *Results Phys.* **2018**, 11, 507.
- [29] M. M. Sabri, J. Jung, D. H. Yoon, S. Yoon, Y. J. Tak, H. J. Kim, *J. Mater. Chem. C* **2015**, 3, 7499.
- [30] S.-I. Park, A.-P. Le, J. Wu, Y. Huang, X. Li, J. A. Rogers, *Adv. Mater.* **2010**, 22, 3062.
- [31] S. de Mulatier, M. Ramuz, D. Coulon, S. Blayac, R. Delattre, *APL Mater.* **2019**, 7, 031505.
- [32] M. M. Hasan, M. Billah, M. N. Naik, *IEEE Electron Device Lett.* **2017**, 38, 1035.
- [33] M. M. Billah, M. M. Hasan, J. Jang, *IEEE Electron Device Lett.* **2017**, 38, 890.
- [34] J. Ni, J. Zhang, J. Xue, X. Wang, L. Cao, C. Wu, S. Xiong, X. Geng, Y. Zhao, *Conf. Rec. 34th IEEE Photovoltaic Spec. Conf. Pennsylvania* **2009**, 293.
- [35] L. Kinner, M. Bauch, R. A. Wibowo, G. Ligorio, E. J. W. List-Kratochvil, T. Dimopoulos, *Mater. Des.* **2019**, 168, 107663.
- [36] Z. Wang, C. Zhang, D. Chen, S. Tang, J. Zhang, Y. Wang, G. Han, S. Xu, Y. Hao, *IEEE Photonics J.* **2015**, 7, 1.
- [37] J. H. Jeong, H. W. Yang, J.-S. Park, J. K. Jeong, Y.-G. Mo, H. D. Kim, J. Song, C. S. Hwang, *Electrochem. Solid-State Lett.* **2008**, 11, H157.
- [38] H.-I. Chen, T.-C. Chang, T.-F. Young, T.-M. Tsai, K.-C. Chang, R. Zhang, S.-Y. Huang, K.-H. Chen, J. C. Lou, M.-C. Chen, C.-C. Shih, S.-Y. Huang, J.-H. Chen, *Appl. Phys. Lett.* **2014**, 104, 243508.
- [39] J. Sheng, T. Hong, H.-M. Lee, K. Kim, M. Sasase, J. Kim, H. Hosono, J.-S. Park, *ACS Appl. Mater. Interfaces* **2019**, 11, 40300.
- [40] P.-T. Liu, Y.-T. Chou, L.-F. Teng, *Appl. Phys. Lett.* **2009**, 95, 233504.
- [41] M. D. H. Chowdhury, S. H. Ryu, P. Migliorato, J. Jang, *J. Appl. Phys.* **2011**, 110, 114503.
- [42] C.-H. Han, S.-S. Kim, K.-R. Kim, D.-H. Baek, S.-S. Kim, B.-D. Choi, *Jpn. J. Appl. Phys.* **2014**, 53, 08NG04.
- [43] Y. Seo, H.-S. Jeong, H.-Y. Jeong, S. Park, J. T. Jang, S. Choi, D. M. Kim, S.-J. Choi, X. Jin, H.-I. Kwon, D. H. Kim, *Materials* **2019**, 12, 3248.
- [44] K. W. Park, G. Jeon, S. Lee, J. B. Ko, S.-H. K. Park, *Phys. Status Solidi A* **2019**, 216, 1800737.
- [45] H. J. Kim, S. Y. Park, H. Y. Jung, B. G. Son, C.-K. Lee, C.-K. Lee, J. H. Jeong, Y.-G. Mo, K. S. Son, M. K. Ryu, S. Lee, J. K. Jeong, *J. Phys. D: Appl. Phys.* **2013**, 46, 055104.
- [46] J. B. Ko, S.-H. Lee, K. W. Park, S.-H. K. Park, *RSC Adv.* **2019**, 9, 36293.
- [47] S. H. Cho, M. K. Ryu, H.-O. Kim, O.-S. Kwon, E.-S. Park, Y.-S. Roh, C.-S. Hwang, S.-H. K. Park, *Phys. Status Solidi A* **2014**, 211, 2126.
- [48] M. Kaltenbrunner, T. Sekitani, J. Reeder, T. Yokota, T. Kuribara, K. Kuribara, T. Tokuhara, M. Drack, R. Schwodiauer, I. Graz, S. Bauer-Gogonea, S. Bauer, T. Someya, *Nature* **2013**, 499, 458.
- [49] J. Kim, J. Hwang, K. Song, N. Kim, J. C. Shin, J. Lee, *Appl. Phys. Lett.* **2016**, 108, 253101.